4-RRS PKM for stabilisation on a mobile sensor platform

Kshir Ramruthan[1*] and *Chioniso* Kuchwa-Dube[2]

[1]Centre for Robotics and Future Production, CSIR, Pretoria, South Africa
[2]School of Mechanical, Industrial & Aeronautical Engineering, University of the Witwatersrand, Johannesburg, South Africa

Abstract. Disturbances experienced by an inspection robot can reduce the quality of its sensor measurements, which can in turn negatively affect the robot's functionality. This research aimed to design a Parallel Kinematic Mechanism (PKM) for use as a stabilisation mechanism. The research focused on designing, simulating, building, testing, and analysing the mechanism. The PKM was modelled and simulated using MATLAB®, designed and developed using NX CAD software, and it was tested using a custom-built test rig that could simulate rotational disturbances. Using the metric of absement, the PKM significantly reduced the disturbances, depending on the disturbance induced.

1 Introduction and background

In the field of robotics, two major areas of study which require stabilisation are camera stabilisation systems [1–3] and platform stabilisation systems on various types of vehicles, such as ships [4–8], land-based vehicles [9,10], and aerial vehicles [11–14].

The Centre for Robotics and Future Production (CRFP), within the Council for Scientific and Industrial Research (CSIR), has developed a mobile robotic platform that can be used in various types of inspection scenarios. Currently, the robot is implemented as a vineyard inspection robot. The significant disturbances caused by the rugged terrain of a vineyard made it necessary to develop a mechanism to provide stabilisation for the robot's sensor platform. A photograph of the inspection robot can be seen in Figure 1.

* Corresponding author: kramruthan@csir.co.za
This work formed part of an MSc(Eng)(Mechanical Engineering) dissertation approved by the University of the Witwatersrand.

Fig. 1. Picture of vineyard inspection robot.

A variety of Parallel Kinematic Mechanisms (PKMs) have been studied for the purpose of stabilisation over the years [4,5,7,10]. Campos et al. [5] describe the use of a Stewart platform as an active helideck to be used on ships or offshore structures. Another study conducted by Madsen et al. [7], studied the design of a Stewart platform to be used as a mounting platform for cranes on ships at sea, for the purpose of wave compensation. PKM designs other than the Stewart platform, and which provide less than six Degrees of Freedom (DoFs), have also been studied for the purpose of stabilisation. Zhang and Shang [4] studied a 3-DoF 3-SRR/SRU (Spherical, Revolute, Revolute/Spherical, Revolute, Universal) PKM design as a stabilisation mechanism for equipment on ships. While the authors Javadi et al. [10] studied the use of a 3-DoF 3-RRS (Revolute, Revolute, Spherical) PKM for the purpose of wheelchair stabilisation. An adapted illustration of the 3-DoF 3-SRR/SRU PKM studied in [4] and the 3-DoF 3-RRS PKM studied in [10] can be seen in Figure 2 a) and b), respectively.

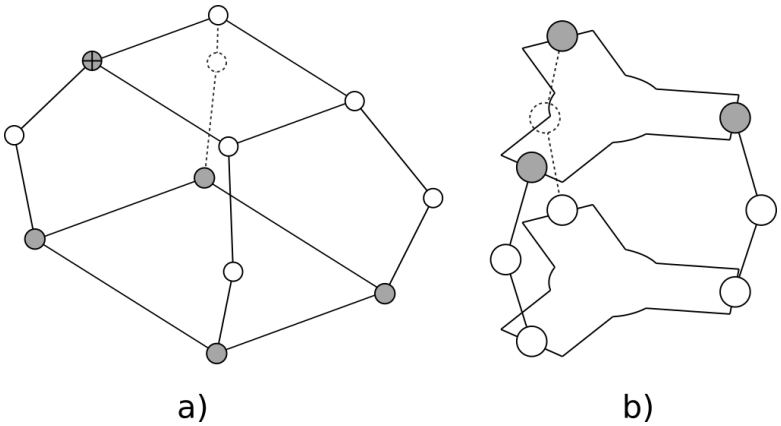

Fig. 2. a) Illustration of 3-DoF 3-SRR/SRU PKM (adapted from [4]); b) Illustration of 3-DoF 3-RRS PKM (adapted from [10])

Many of the PKMs studied in literature are non-redundant PKMs. For the study at hand, the design of a redundantly actuated PKM was of interest due the benefits it could provide.

A redundantly actuated PKM has more active joints than its number of DoFs [15,16]. The benefits of actuation redundancy can include reducing or even eliminating singularities, increasing carrying capacity, increasing stiffness, and improving joint-torque distributions [15]. Although redundancy can provide several benefits, it can also bring about additional challenges, such as the generation of internal forces which can lead to control complexities and increased complexity in terms of calibration [15].

This paper consists of five sections. Section 2 describes the design and simulation of a PKM proposed for the stabilisation of the sensor platform of the mobile inspection robot. Section 3 details the process of building and testing the PKM as well as the results found from the various tests conducted. Section 4 concludes the paper, and finally Section 5 presents possible areas of future work.

2 Design and simulation

As mentioned earlier, a current implementation of the robotic platform is as a vineyard inspection robot, where the rugged terrain of the vineyard introduces significant disturbances to the sensor platform of the robot. There are three movements of the sensor platform that require stabilisation, these are, roll (rotation about the x-axis), pitch (rotation about the y-axis), and vertical translation (translation about the z-axis). Figure 3 illustrates the movements of the sensor platform that require stabilisation.

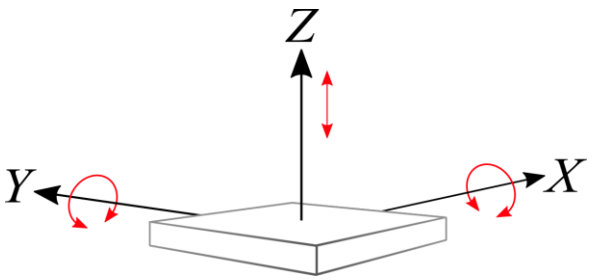

Fig. 3. Illustration of sensor platform movements requiring stabilisation

The following sections describe the design of the proposed PKM for stabilisation of the sensor platform as well as the calculation of the PKM's inverse kinematics. It then goes on to describe the various simulations conducted and the insight gathered from the different simulations.

2.1 PKM description and inverse kinematics

After considering the various PKM designs studied in literature and the benefits of actuation redundancy, a 3-DoF 4 Revolute, Revolute, Spherical (4-RRS) redundantly actuated PKM is proposed. The 3-DoFs provided by the PKM are roll, pitch, and vertical translation. The 4-RRS PKM consists of a fixed base, four arms, and a moving end-effector. Each arm connects the base to the end-effector via an actuated revolute joint at B_i $\{i = 1, 2, 3, 4\}$, an arm consisting of two parts (lower arm and upper arm) connected by a revolute joint, and a spherical joint at A_i $\{i = 1, 2, 3, 4\}$. An illustration of the design is depicted in Figure 4.

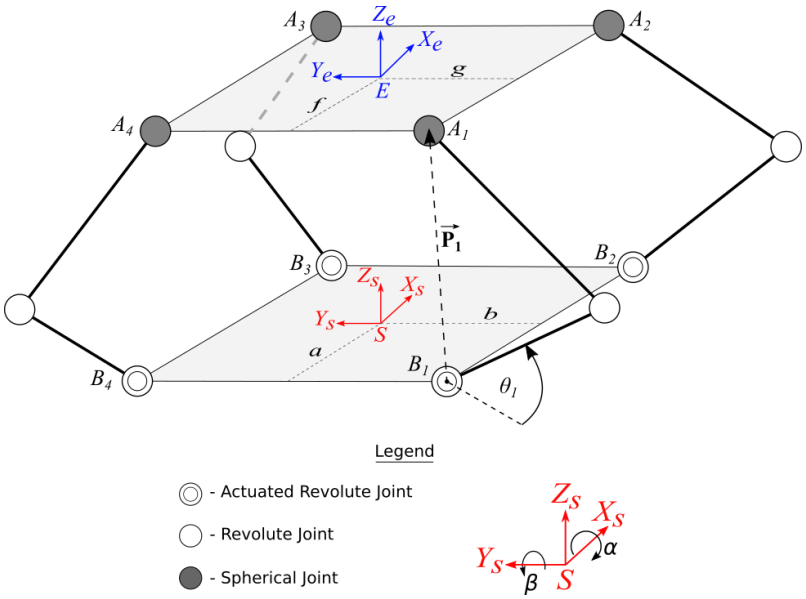

Fig. 4. Illustration of 4-RRS PKM

The inverse kinematics of a PKM can be determined using several different techniques. The vector loop method is a common technique used [17] and was chosen as the technique for determining the inverse kinematics of this 4-RRS mechanism. The methods used in [18], [17], [4], and [19] were utilised for the calculation of the inverse kinematics of the 4-RRS mechanism.

A fixed co-ordinate frame referred to as the Space frame S{X_s, Y_s, Z_s} is defined at the centre of the base platform and a moving co-ordinate frame E{X_e, Y_e, Z_e} is defined at the centre of the end-effector platform. Angles α and β are defined as two independent angles which represent the rotation of the end-effector frame, first about the x-axis by α degrees, then about the y-axis by β degrees, according to the right-hand rule.

Using the definitions above, the rotation matrix of the platform relative to the base, R_{SE}, is defined as:

$$R_{SE} = \begin{bmatrix} \cos(\beta) & \sin(\alpha)\sin(\beta) & \cos(\alpha)\sin(\beta) \\ 0 & \cos(\alpha) & -\sin(\alpha) \\ -\sin(\beta) & \sin(\alpha)\cos(\beta) & \cos(\alpha)\cos(\beta) \end{bmatrix} \quad (1)$$

Since the translation of the end-effector frame is given only by translation along the z-axis, the translation matrix d is defined as:

$$d = \begin{bmatrix} 0 \\ 0 \\ d_z \end{bmatrix} \quad (2)$$

Combining the rotation matrix, R_{SE}, from equation (1) and translation matrix, d, from equation (2), the homogeneous transformation matrix, T_{SE}, is defined as:

$$T_{SE} = \begin{bmatrix} R_{SE} & d \\ 0 & 1 \end{bmatrix} \quad (3)$$

From Figure 4, the co-ordinates of the vertices on the base platform are determined with respect to the fixed frame, *S*, as:

$$B_1 = \begin{bmatrix} -a \\ -b \\ 0 \end{bmatrix},\ B_2 = \begin{bmatrix} a \\ -b \\ 0 \end{bmatrix},\ B_3 = \begin{bmatrix} a \\ b \\ 0 \end{bmatrix},\ B_4 = \begin{bmatrix} -a \\ b \\ 0 \end{bmatrix} \quad (4)$$

The vertices on the end-effector are determined with respect to the moving frame, E, as:

$${}^{E}A_1 = \begin{bmatrix} -f \\ -g \\ 0 \end{bmatrix},\ {}^{E}A_2 = \begin{bmatrix} f \\ -g \\ 0 \end{bmatrix},\ {}^{E}A_3 = \begin{bmatrix} f \\ g \\ 0 \end{bmatrix},\ {}^{E}A_4 = \begin{bmatrix} -f \\ g \\ 0 \end{bmatrix} \quad (5)$$

Note that the left superscript of a vertex indicates the frame in which it is being represented, and that if a vertex does not have a left superscript, then it is being represented in the fixed frame *S*.

The vertices, ${}^{E}A_i$, on the end-effector can be represented in the fixed frame, *S*, by pre-multiplying them by the homogeneous transformation matrix T_{SE} as follows:

$$\begin{bmatrix} A_i \\ 1 \end{bmatrix} = T_{SE} \begin{bmatrix} {}^{E}A_i \\ 1 \end{bmatrix},\ \mathrm{i} = 1,\ 2,\ 3,\ 4 \quad (6)$$

With the vertices of the base and end-effector both represented in the fixed frame, S, the vector $\vec{\mathbf{P}}_\mathbf{i}$ can be calculated as follows:

$$\vec{\mathbf{P}}_\mathbf{i} = A_i - B_i,\ i = 1,\ 2\ ,\ 3,\ 4 \quad (7)$$

Finally, using vector loop analysis, trigonometry, and the cosine rule, the actuation variable, θ_i, is found as:

$$\theta_i = \pi - \left[\arcsin\left(\frac{P_{iz}}{|P_i|}\right) + \arccos\left(\frac{|P_i|^2 + l_1^2 - l_2^2}{2|P_i|l_1}\right)\right], i = 1, 2, 3, 4 \quad (8)$$

Where P_{iz} is the z co-ordinate of the vector $\vec{\mathbf{P}}_\mathbf{i}$ and l_1 and l_2 are the lengths of the lower arm and upper arm, respectively.

2.2 Simulation

The proposed 4-RRS PKM was simulated using MATLAB®. Three types of simulations were conducted, with the difference between each type of simulation being the way in which the arms of the mechanism function. The simulations were developed using methods similar to those used in [20].

For the first simulation, the PKM was simulated under the assumption that it would be able to provide the 3-DoFs required, while the base platform and arms remained within their defined planes. However, this assumption was found to be incorrect, leading to simulations 2 and 3, which aimed to provide solutions to the problem discovered in simulation 1. The second simulation allowed for each arm of the PKM to rotate between points A_i and B_i to accommodate for the movement of the end-effector. The third simulation constrained the lower arm (l_{1i}) to the plane in which it is attached at the base, while allowing the upper arm (l_{2i}) to leave this plane to accommodate the movement of the end-effector.

2.2.1 Simulation 1 – Assumption that PKM remains rigid

Simulation 1 simulated the 4-RRS PKM under the assumption that the mechanism would be able to provide the 3-DoFs required, while the base platform and arms remained within their defined planes. This assumption was found to be incorrect as rolling or pitching motions of the end-effector caused the upper arms (l_{2i}) of the mechanism to rotate out of their defined plane and deform slightly, in order to accommodate the motion. Vertical translations on the other hand, did not result in any deformation. Two possible solutions to this problem were investigated by conducting simulations 2 and 3.

2.2.2 Simulation 2 – Arms allowed to rotate between points A_i and B_i

As a possible solution to the problem identified in simulation 1, simulation 2 allowed each arm to rotate between points A_i and B_i to accommodate the movements of the end-effector, without having any part of the mechanism deform. This simulation resulted in the PKM being able to either roll or pitch by a maximum angle of approximately ±38°. Figure 5 depicts the top view of the PKM after performing a roll of +38°, showing how the arms have rotated out of their initial reference planes.

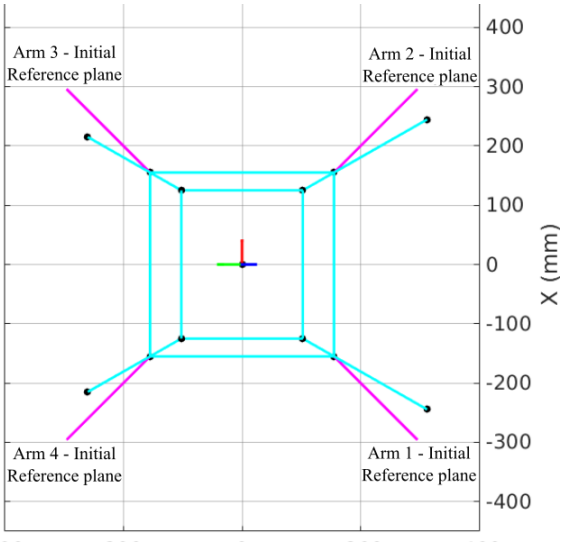

Fig. 5. Simulation 2 - Animation of 4-RRS PKM after performing roll of +38° (top view)

From simulation 2, it was determined that the arms would have to be able to rotate approximately ±16.5° from their initial reference plane to accommodate a roll or pitch of ±38°. This amount of movement was viewed as being rather significant and likely to increase the complexity of the mechanism from both an implementation and control perspective. Simulation 3 was therefore conducted to investigate a second design which could provide a more feasible solution for implementation while still achieving the required movement of the end-effector.

2.2.3 Simulation 3 – Lower arm constrained and upper arm unconstrained

As another possible solution to the problem identified by simulation 1, simulation 3 constrained the lower arms (l_{1i}) of the platform to the plane in which they are attached to the base of the platform (which is in-line with the diagonal of the base), while allowing the upper

arms (l_{2i}) to leave the plane to accommodate for the motion of the end-effector. Put simply, simulation 3 simulated the PKM as if the revolute joint that joins the lower and upper parts of each arm had some amount of flexibility. This flexibility is required to allow the upper arms (l_{2i}) to leave the plane in which the lower arms (l_{1i}) are constrained, allowing the end-effector to pitch or roll. Similarly to simulation 2, simulation 3 resulted in the PKM being able to either roll or pitch by a maximum angle of approximately ±38°. Figure 6 depicts the top view of the PKM after performing a roll of +38°, showing how the upper arms have rotated out of the plane that the lower arms are constrained to.

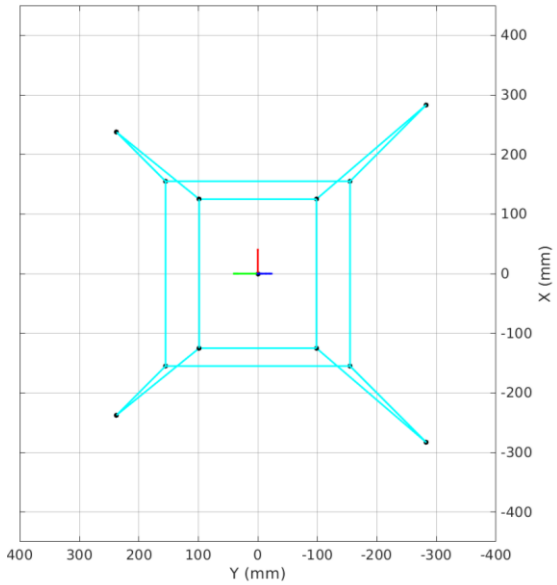

Fig. 6. Simulation 3 - Animation of 4-RRS PKM after performing roll of +38° (top view)

From simulation 3, it was found that the upper arms would have to be allowed to move ±6.6° out of the plane in which the lower arms are constrained, to accommodate a roll or pitch of ±38°. This amount of movement is significantly less than that required by simulation 2, and it could be achieved by using a flexible material, with restorative properties, within the revolute joint that connects the lower and upper arm.

Since simulation 3 allows the upper arm to leave the plane in which the lower arm is constrained, the inverse kinematic equations which were calculated are not a true representation of how the PKM behaves in this simulation. Therefore, the simulation also calculated the deviation of the actuation angle (θ_i) calculated using the inverse kinematic equations versus the actual actuation angle found in the simulation. It was found that the maximum deviation between the actuation angle calculated using the inverse kinematic equations and the actuation angle calculated by the simulation, was approximately 0.6°. Using this maximum angle by which the actuation angle could deviate, the maximum angle by which the end-effector could deviate (due to the actuation deviation) was found to be approximately 1.33°. Since the project at hand required that the sensor platform be kept within a position tolerance of ±4°, this maximum end-effector deviation was deemed to be acceptable. It was therefore decided that the PKM would be physically implemented according to simulation 3 (i.e. having a slightly flexible revolute joint between the lower and upper arm), while it would be controlled using the kinematic equation given in equation (8).

3 Build, testing, and results

The following sections detail the mechanical design and manufacture of the PKM, as well as the electronics and software used. It then goes on to describe the testing methods used and the results that were recorded.

3.1 Build

3.1.1 PKM design and manufacture

The PKM that would be required for the mobile inspection robot was designed using Siemens NX CAD software, and a 50% scale model of the PKM was built for testing. Using this CAD design and a waterjet cutter, the various components, such as the base, arms, and the end-effector were manufactured by cutting them out of varying thicknesses of aluminium. The lower arms were then machined into their required shape. The lower arms were also designed to allow for rubber foam to be inserted into the revolute joint to allow for the flexibility required for the design to work. NX was also used to design the spherical joints of the PKM. The spherical joints were designed to help optimise the amount of movement the end-effector is capable of, and they were 3D printed using a resin printer. Figure 7 A) depicts a render of the 4-RRS PKM while Figure 7 B) depicts the physical 4-RRS PKM that was built.

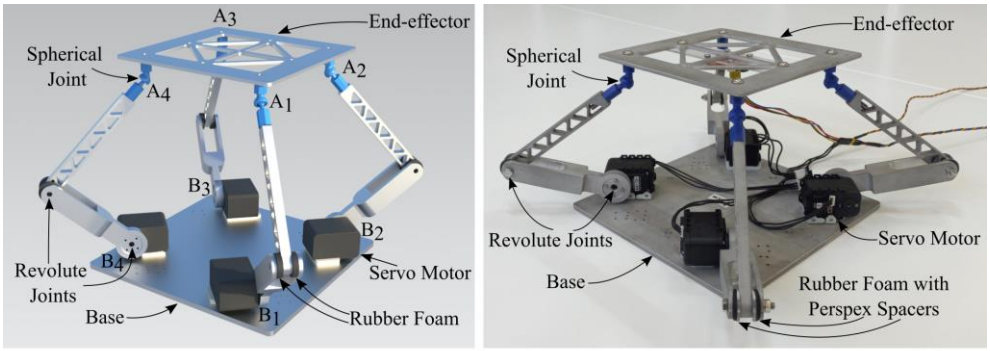

Fig. 7. A) 4-RRS PKM CAD rendering, B) Photo of the physical 4-RRS PKM

The PKM uses Dynamixel AX-12+ servo motors for each of the actuated revolute joints. A 9-DoF Razor M0 Inertial Measurement Unit (IMU) is attached to the bottom of the end-effector for pose tracking, and an Arduino Due is used as the processing unit that controls the PKM.

3.1.2 Test rig design and manufacture

In order to test the ability of the 4-RRS PKM to keep the end-effector stable when disturbances are induced at its base, a simple test rig was developed. By using the test rig, it allows for a variety of tests to be performed on the PKM in a controlled environment. The test rig consists of a stepper motor with a gearbox, motor controller, encoder, platform for mounting the PKM, and Arduino Mega which controls the test rig. Figure 8 A) depicts the test rig setup used to simulate a rotation about a single axis (roll or pitch) of the PKM, while Figure 8 B) depicts the test rig setup used to simulate rotation about both axes (roll and pitch)

of the PKM, simultaneously. The combined roll and pitch rotation of the PKM is achieved by rotating the PKM about its diagonal.

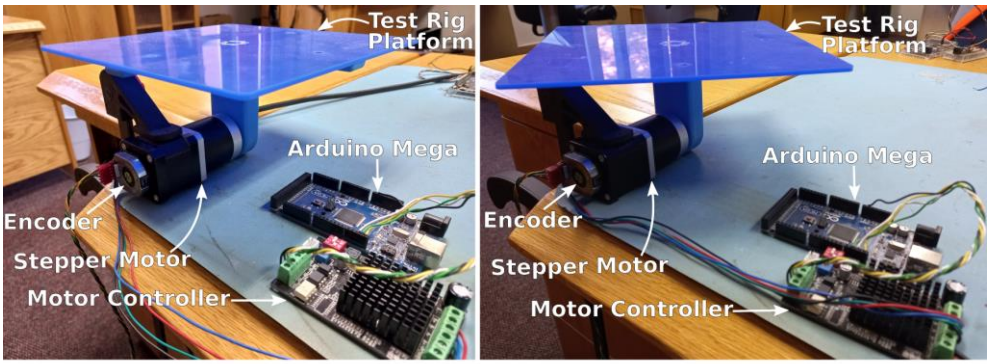

A) B)

Fig. 8. Test rig setup for A) Single axis rotation and B) Combined axes rotation.

3.1.3 Pose tracking

To keep the end-effector stable, its pose (position and orientation) needs to be constantly monitored so that any changes can be corrected. Orientation tracking is often implemented by using an IMU, where the different sensor measurements can be fused to give more accurate orientation estimates than those that would be calculated by using only one of the sensor measurements [21]. There are several sensor fusion algorithms that can be used for orientation tracking, such as the complementary filter, the Mahony filter, the Madgwick filter, and the extended Kalman filter, to name a few. From literature, the Madgwick and Mahony filters have been shown to produce relatively similar results to each other [22] as well as extended Kalman filters, while requiring low computational loads [21,23,24]. They were therefore chosen as potential sensor fusion algorithms for the project at hand, as the PKM uses an embedded processing unit that is resource constrained.

To choose between the Madgwick and Mahony filters, an IMU was mounted onto the test rig. Three tests were then conducted where data was collected from the IMU while the test rig induced a rotation about a single axis of the IMU, at the test rig's maximum speed. To compare the Madgwick and Mahony algorithms to each other, they were both applied to the three datasets collected, and their Root Mean Square Errors (RMSEs) were then calculated. The position feedback provided by the encoder of the test rig was used as the reference for the calculation of the RMSE of each algorithm. As seen in Table 1, the Madgwick filter performed slightly better than the Mahony filter, with the Madgwick filter having an average RMSE value of 0.89° while the Mahony filter had an average RMSE value of 0.99°. The Madgwick filter was therefore chosen as the algorithm to be used for the orientation tracking of the end-effector of the PKM.

Table 1. Root Mean Square Error (RMSE) for the Madgwick and Mahony filters (in degrees)

	Test 1	**Test 2**	**Test 3**	**Average**
Madgwick	0.73	0.73	1.22	0.89
Mahony	0.86	0.81	1.29	0.99

An attempt was made to use the IMU, used for orientation tracking of the end-effector, for position tracking as well. However, unlike orientation tracking which can fuse measurements from the accelerometer and gyroscope to improve the accuracy of orientation

estimates, position tracking using an IMU typically relies on the accelerometer measurements alone and is less accurate. Low cost IMUs can only be used for velocity and position estimates for a few seconds before the growth of unbounded errors corrupts the estimates [25,26].

To help bound the position estimation errors the Zero Velocity Update (ZUPT) method was implemented. The ZUPT method is often used in the human motion tracking field of research [27,28]. The ZUPT method involves detecting stationary periods, by comparing accelerometer or velocity measurements to certain thresholds. The detection of these stationary periods allows for the velocity measurement to be forced to zero and any accelerations or velocities detected during this period are assumed to be an error and are ignored [27]. This helps avoid discontinuities in the measurements and helps bound errors in the estimates [27].

After implementing the ZUPT algorithm, several tests were conducted to assess the accuracy and reliability of the position estimations. These tests showed that even with the implementation of the ZUPT algorithm, the position estimates of the end-effector were often inaccurate and unreliable. A possible reason for the low accuracy and reliability of the position estimates could be attributed to the grade of the IMU sensor used. One of the main factors that contribute to errors in the ZUPT method is IMU noise [29]. Low-cost consumer grade Micro-Electro-Mechanical Systems (MEMS) IMUs, like the one used in this project, often suffer from high noise levels [29] and offer lower performance compared to tactical or navigational grade IMUs [30,31]. A possible explanation for why the ZUPT method may not perform here as well as it performs in human gait tracking research, is that studies on the human gait typically use a detectable event that occurs during walking (such as the heel striking the ground) to aid the ZUPT algorithm or help determine the thresholds to use [27–29]. For the project at hand, the movements of the PKM can be completely random and it can occur at varying speeds, there are therefore no known detectable events that can be used to aid the ZUPT algorithm, like with human gait tracking. This makes it significantly difficult to "tune" the ZUPT algorithm for the detection of stationary periods.

3.1.4 Control strategy

A classical control approach was taken for this project, as many other PKMs studied in literature have taken the same approach [4,5,10,32], and classical control is still a relevant control strategy in this field of research [33]. The 4-RRS PKM requires three parameters to be controlled, these are roll, pitch, and vertical translation. To accomplish this, three PID controllers were used, one to control each parameter. It is worth noting that the controller responsible for the control of the vertical translation was disabled during all tests, since the position of the end-effector could not be reliably tracked, as mentioned in Section 3.1.3. The controllers for the roll and pitch of the PKM were tuned experimentally.

3.2 Testing

Two types of tests were conducted on the 4-RRS PKM, these were step response tests and test rig tests. The following sections aim to describe these two tests in detail.

3.2.1 Step response tests

For the step response tests the base of the 4-RRS PKM is securely fastened to the table on which the tests are being conducted. The PKM control software is setup for a step response test, which would first perform an initialisation procedure, then once the PKM is initialised, the setpoint of the orientation/s being tested is changed to a predefined step value. The response to this change is then recorded for analysis.

3.2.2 Test rig tests

For the test rig tests, the base of the PKM is securely fastened to the test rig platform, the test rig is then securely fastened to the table on which the tests are being conducted. The PKM control software is setup for a test rig test, which would first perform an initialisation procedure, then once the initialisation is completed, the PKM controller signals the test rig controller to begin the test.

A test rig test consists of the test rig platform rotating from the horizontal position, which is regarded as 0°, to +25°, pausing for 100 milliseconds, then rotating back to 0°, pausing for another 100 milliseconds, then rotating to -25°, pausing for another 100 milliseconds, before finally rotating back to 0°. This test is meant to simulate the inspection robot driving over a bump. Using the scenario of the inspection robot driving over a bump at its maximum forward velocity, the maximum angular velocity that would be required by the PKM was calculated. Using the maximum angular velocity required by the PKM, three speed settings were defined for the test rig tests. These speed settings were low speed, moderate speed, and high speed. Low speed tests involve the test rig rotating at approximately 10% of the maximum angular velocity required and are equal to a rotation of approximately 7.11°/s. Moderate speed tests involve the test rig rotating at approximately 50% of the maximum angular velocity required and are equal to a rotation of approximately 35.27°/s. High speed tests involve the test rig rotating at approximately 100% of the maximum angular velocity required and are equal to a rotation of approximately 70.16°/s.

It is worth noting that for single axis rotations, which is when either the roll or pitch axis is aligned with the axis of rotation of the test rig, the full magnitude of the disturbance induced by the test rig is transferred to the PKM axis being tested. However, for combined axes rotations, approximately 70% of the magnitude of the disturbance induced by the test rig is transferred to the roll and pitch axes, this is because of the offset between the roll and pitch axes with the axis of rotation of the test rig. During a test rig test, various PKM state information and test rig position information is recorded by a PC for analysis at a later stage.

3.3 Results

The following sections present the results obtained from the various step response tests and test rig tests that were conducted.

3.3.1 Step response test results

A total of 9 unloaded step response tests were conducted. These tests are referred to as unloaded because the end-effector had no payload or additional weight attached to it when the tests were conducted. These tests were conducted according to the procedure outlined in section 3.2.1 and consisted of 3 roll tests, 3 pitch tests, and 3 combined roll and pitch tests. An angle of 12° was used as the step input for all tests and the PID gains for both the roll and pitch controllers were: K_p = 0.5, K_i = 3.5, and K_d = 0.005. Figure 9 provides a graph of the step responses measured for the unloaded pitch tests, while Table 2 provides the average rise times, percentage overshoot, and settling times calculated from the various step response tests conducted.

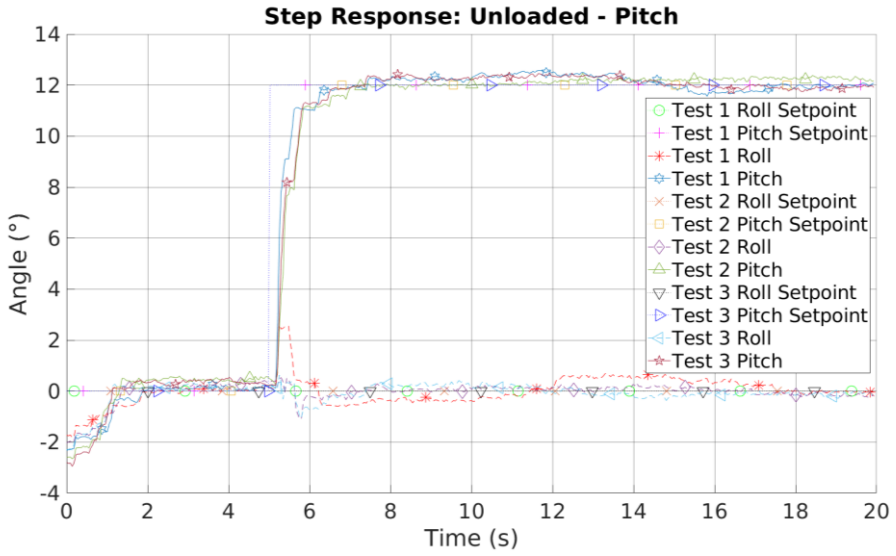

Fig. 9. Plot of step responses for unloaded pitch tests

Table 2. Average rise times, percentage overshoot, and settling times of the step response tests conducted.

Test type	Average		
	Rise time (s)	Overshoot (%)	Settling time (s)
Roll	0.739	6.73	6.462
Pitch	0.528	4.03	1.341
Roll (combined test)	0.828	4.53	1.921
Pitch (combined test)	0.449	3.97	0.732

From Table 2 it is seen that the 4-RRS PKM performed well to step inputs, be it in terms of roll, pitch, or combined roll and pitch. The average rise time of all tests was below 0.830 seconds. The largest average percentage overshoot was 6.73%, which translates to an overshoot value of approximately 0.81°. Finally, the average settling time for the roll test was found to be the largest settling time at 6.462 seconds, however all other tests produced an average settling time of less than 2 seconds.

3.3.2 Test rig test results

A total of 9 unloaded test rig tests were conducted. These tests are referred to as unloaded because the end-effector had no payload or additional weight attached to it when the tests were conducted. These tests were conducted according to the procedure outlined in section 3.2.2 and consisted of a roll, pitch, and combined roll and pitch test occurring at the low speed, moderate speed, and high speed settings of the test rig. Figure 10 provides a graph of the results obtained for the unloaded roll test that was performed at low speed. Tables 3, 4, and 5 present the metrics calculated for the various tests that were conducted at low speed, moderate speed, and high speed, respectively.

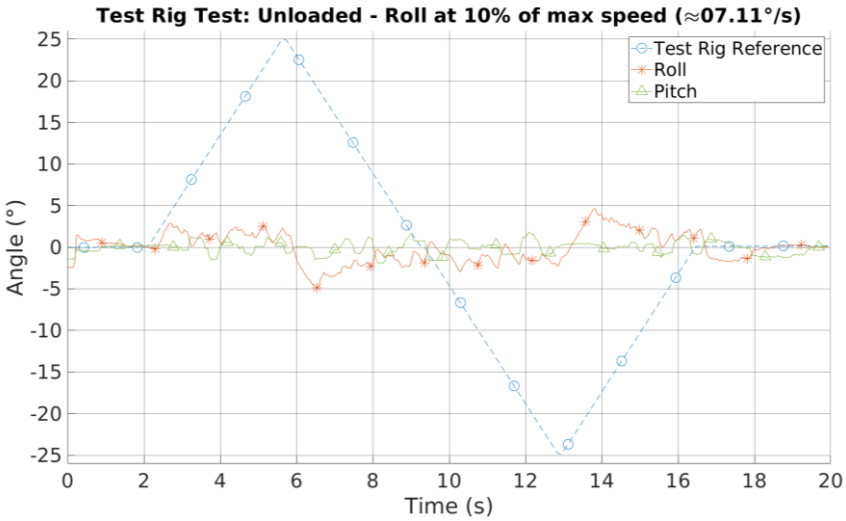

Fig. 10. Test rig test results for a roll at low speed.

Table 3. Metrics calculated for test rig tests conducted at low speed.

Test type	Maximum positive angle (°)	Maximum negative angle (°)	Ratio of end-effector to disturbance time spent outside ±4° threshold	Absement reduction (%)
Roll	4.7	-4.9	0.04	99.84
Pitch	5.4	-4.8	0.06	99.74
Roll (combined test)	3.4	-3.2	0.00	100.00
Pitch (combined test)	3.9	-2.8	0.00	100.00

Table 4. Metrics calculated for test rig tests conducted at moderate speed.

Test type	Maximum positive angle (°)	Maximum negative angle (°)	Ratio of end-effector to disturbance time spent outside ±4° threshold	Absement reduction (%)
Roll	13.6	-14.5	0.96	56.35
Pitch	13.5	-14.7	1.02	56.32
Roll (combined test)	8.7	-8.9	0.80	76.23
Pitch (combined test)	9.3	-9.5	0.88	72.86

Table 5. Metrics calculated for test rig tests conducted at high speed.

Test type	Maximum positive angle (°)	Maximum negative angle (°)	Ratio of end-effector to disturbance time spent outside ±4° threshold	Absement reduction (%)
Roll	22.4	-22.8	1.17	3.66
Pitch	21.9	-23.5	1.07	4.06
Roll (combined test)	17.7	-16.1	1.14	2.74
Pitch (combined test)	17.1	-15.7	1.21	0.98

Tables 3, 4, and 5 present the different metrics calculated for the various tests conducted at the different speeds. The maximum positive/negative angle metric is simply the maximum positive/negative angle that was experienced by the end-effector during the test. The ratio of end-effector to disturbance time spent outside ±4° threshold metric, is the ratio of the time spent by the end-effector outside the project's position tolerance of ±4°, compared to the disturbance that was induced during the test. Lastly, the absement reduction is the percentage by which the PKM reduced the end-effectors absement, compared to the absement of the disturbance induced. Absement is the time integral of displacement and it can be used to measure deviation/error from some reference position that needs to be maintained [34]. Note that the absement values were calculated for all periods where the end-effector or induced disturbance angle exceeded the project's position tolerance of ±4°.

For all single roll or pitch tests the average maximum disturbance induced was approximately ±24.97°, while the average maximum disturbance induced on either the roll or pitch axis for all combined tests was approximately ±17.37°. Using this information and the information presented in Tables 3, 4, and 5, it can be seen that, with the exception of the roll response for the combined test conducted at high speed, the maximum angle transferred to the end-effector of the 4-RRS PKM was always smaller than the disturbance induced.

In terms of the amount of time the end-effector spent outside the acceptable position tolerance, the PKM performed well for the tests conducted at low speed. For the moderate speed tests, the 4-RRS PKM was much less effective in reducing the amount of time the end-effector spent outside the acceptable position tolerance. For the high speed tests, the PKM unfortunately caused a moderate increase in the time the end-effector spent outside the acceptable position tolerance.

Finally, from Tables 3, 4, and 5 it can be seen that the PKM was always able to reduce the absement of the PKMs end-effector compared to the absement of the disturbance induced. The range of absement percentage reduction for low speed tests was 99.74% to 100%, for moderate speed tests it was 56.32% to 76.23%, and for high speed tests it was 0.98% to 4.06%.

4 Conclusion

This paper proposes the use of a 4-RRS PKM for the stabilisation of the sensor platform of a mobile inspection robot. The PKM structure was defined, and the inverse kinematic equations calculated. Simulating the PKM found that it would require the centre revolute joint of each arm to be slightly flexible in order to provide the required roll and pitch motions. Using the inverse kinematic equations and information gathered from the simulations, the PKM was built and tested. Unfortunately, the vertical translation of the end-effector could not be reliably measured, which meant that the PKMs ability to control the vertical translation of the end-effector could not be tested. The 4-RRS PKM has shown that it performs well to step

input tests. The test rig tests, which were used for the analysis of the 4-RRS PKM's ability to isolate the end-effector from disturbances that would be experienced by the inspection robot, showed that the PKM responds well to disturbances induced at low to moderate speeds. Overall, the 4-RRS PKM has shown that it is a possible solution for the stabilisation of the sensor platform of the mobile inspection robot.

5 Future work

Future work for this research could entail the calculation of the inverse kinematics, which considers the flexibility of the centre revolute joints. Having the more accurate inverse kinematics can lead to more accurate positioning of the end-effector and allow for further static and dynamic analyses of the PKM to be done. Another area that could be investigated further, is the application of a higher grade IMU, such as tactical or navigational grade, for the tracking of the end-effectors vertical translation. Other algorithms or methods for position tracking could also be investigated. Finally, it was noted that the restorative properties of the rubber foam, which was used in the revolute joints, would diminish over time, affecting the performance of the PKM. Research into better materials, with better resilience, or even better mechanisms that could be used to provide the flexibility required, could also form part of future work.

References

1. R. J. Rajesh and P. Kavitha, “Camera gimbal stabilization using conventional PID controller and evolutionary algorithms,” in *2015 International Conference on Computer, Communication and Control (IC4)*, (2015).
2. F. Königseder, W. Kemmetmüller, and A. Kugi, “Attitude control strategy for a camera stabilization platform,” *Mechatronics* **46**, 60–69 (2017).
3. W. Günthner, P. Wagner, and H. Ulbrich, “An inertially stabilised vehicle camera system - Hardware, algorithms, test drives,” in *IECON 2006 - 32nd Annual Conference on IEEE Industrial Electronics*, (2006).
4. B. Zhang and W. Shang, “Kinematic control of a 3-DOF parallel stabilization platform,” in *Proceedings of the 33rd Chinese Control Conference*, (2014).
5. A. Campos, J. Quintero, R. Saltarén, M. Ferre, and R. Aracil, “An active helideck testbed for floating structures based on a stewart-gough platform,” in *2008 IEEE/RSJ International Conference on Intelligent Robots and Systems*, (2008).
6. X. Liu, T. Zhao, E. Luo, W. Chen, and Q. Pan, “Coupling 3-PSR/PSU 5-axis compensation mechanism for stabilized platform and its analysis,” *Proc Inst Mech Eng C J Mech Eng Sci* **227**, 1619–1629 (2013).
7. A. L. Madsen and S. G. Kristensen, “Design of Stewart Platform for Wave Compensation,” Masters Thesis (2012).
8. J. Guo, G. Li, B. Li, and S. Wang, “A ship active vibration isolation system based on a novel 5-DOF parallel mechanism,” in *2014 IEEE International Conference on Information and Automation (ICIA)*, (2014).
9. A. Strydom and S. Els, “Vibration isolation analysis of a stabilized platform mounted on a small off-road vehicle,” in *9th South African Conference on Computational and Applied Mechanics, SACAM 2014*, (2014).
10. M. Javadi, N. Afzalpour, P. Jafari Taayemeh, and S. M. Khorsandijou, “Wheelchair Stabilization by the Control of a Spatial 3-RRS Mechanism,” *Iranian Journal of Mechanical Engineering* **17**, 83–99 (2016).

11. L. Zhuchong, L. Kun, and Z. Wei, "Inertially Stabilized Platform for Airborne Remote Sensing Using Magnetic Bearings," *IEEE/ASME Transactions on Mechatronics* **21**, 288–301 (2016).
12. D. K. Nikulin, "Active stabilization of an antenna system," *Journal of Machinery Manufacture and Reliability* **36**, 110–113 (2007).
13. M. Dunbabin, S. Brosnan, J. Roberts, and P. Corke, "Vibration isolation for autonomous helicopter flight," in *IEEE International Conference on Robotics and Automation*, (2004).
14. C. R. Maj, "A novel approach to vibration isolation in small, unmanned aerial vehicles," in *2009 IEEE International Conference on Technologies for Practical Robot Applications*, (2009).
15. M. Luces, J. K. Mills, and B. Benhabib, "A Review of Redundant Parallel Kinematic Mechanisms," *J Intell Robot Syst* **86**, 175–198 (2017).
16. D. Zhang, Q. Shi, and J. Li, "A comparison study of three degree-of-freedom micro-motion parallel kinematic machines with/without actuation redundancy," in *2010 International Conference on Manufacturing Automation*, (2010).
17. C. Zhang and L. Zhang, "Kinematics analysis and workspace investigation of a novel 2-DOF parallel manipulator applied in vehicle driving simulator," *Robot Comput Integr Manuf* **29**, 113–120 (2013).
18. K. Liu, J. M. Fitzgerald, and F. L. Lewis, "Kinematic analysis of a Stewart platform manipulator," *IEEE Transactions on Industrial Electronics* **40**, 282–293 (1993).
19. S. Zarkandi, "Kinematics and singularity analysis of a parallel manipulator with three rotational and one translational DOFs," *Mechanics Based Design of Structures and Machines* **39**, 392–407 (2011).
20. S. T. Marais, "The development of a haptic feedback system for vision-assisted hexapod robot foot placement," PhD Thesis (2017).
21. S. A. Ludwig and K. D. Burnham, "Comparison of Euler Estimate using Extended Kalman Filter, Madgwick and Mahony on Quadcopter Flight Data," in *2018 International Conference on Unmanned Aircraft Systems (ICUAS)*, (2018).
22. S. A. Ludwig, "Optimization of Control Parameter for Filter Algorithms for Attitude and Heading Reference Systems," in *2018 IEEE Congress on Evolutionary Computation (CEC)*, (2018).
23. S. O. H. Madgwick, A. J. L. Harrison, and R. Vaidyanathan, "Estimation of IMU and MARG orientation using a gradient descent algorithm," in *2011 IEEE International Conference on Rehabilitation Robotics*, (2011).
24. P. J. Kieliba, P. H. Veltink, T. Lisini Baldi, D. Prattichizzo, G. Santaera, A. Bicchi, M. Bianchi, and B. J. F. Van Beijnum, "Comparison of Three Hand Pose Reconstruction Algorithms Using Inertial and Magnetic Measurement Units," in *2018 IEEE-RAS 18th International Conference on Humanoid Robots (Humanoids)*, (2018).
25. G. Baldwin, R. Mahony, J. Trumpf, T. Hamel, and T. Cheviron, "Complementary filter design on the Special Euclidean group SE(3)," in *2007 European Control Conference (ECC)*, (2007).
26. M. Bryson and S. Sukkarieh, "Vehicle Model Aided Inertial Navigation for a UAV using Low-cost Sensors," in *Australasian Conference on Robotics and Automation*, (2004).
27. K. Abdulrahim, T. Moore, C. Hide, and C. Hill, "Understanding the Performance of Zero Velocity Updates in MEMS-based Pedestrian Navigation," *International Journal of Advancements in Technology* **5**, 53–60 (2014).

28. J. C. Alvarez, A. M. López, R. C. González, and D. Álvarez, "Pedestrian dead reckoning with waist-worn inertial sensors," in *2012 IEEE International Instrumentation and Measurement Technology Conference Proceedings*, (2012).
29. Y. Wang, A. Chernyshoff, and A. M. Shkel, "Study on estimation errors in ZUPT-Aided pedestrian inertial navigation due to IMU noises," *IEEE Trans Aerosp Electron Syst* **56**, 2280–2291 (2020).
30. X. Niu, Q. Wang, Y. Li, Q. Zhang, and P. Jiang, "An IMU evaluation method using a signal grafting scheme," *Sensors* **16**, 1–21 (2016).
31. N. El-Sheimy and A. Youssef, "Inertial sensors technologies for navigation applications: state of the art and future trends," *Satellite Navigation* **1**, 1–21 (2020).
32. P. Lambert, "Parallel Robots with Configurable Platforms," PhD Thesis (2013).
33. R. P. Borase, D. K. Maghade, S. Y. Sondkar, and S. N. Pawar, "A review of PID control, tuning methods and applications," *Int J Dyn Control* **9**, 818–827 (2021).
34. S. Mann, C. Pierce, B. C. Zheng, J. Hernandez, C. Scavuzzo, and C. Mann, "Integral kinesiology feedback for weight and resistance training," in *2019 15th International Conference on Signal-Image Technology & Internet-Based Systems (SITIS)*, (2019).